



Research Repository UCD

Title	Micromagnet arrays for on-chip focusing, switching, and separation of superparamagnetic beads and single cells
Authors(s)	Rampini, Stefano, Kilinc, Devrim, Li, Peng, Monteil, C., Gandhi, Dhruv, Lee, Gil U.
Publication date	2015-07-10
Publication information	Rampini, Stefano, Devrim Kilinc, Peng Li, C. Monteil, Dhruv Gandhi, and Gil U. Lee. "Micromagnet Arrays for On-Chip Focusing, Switching, and Separation of Superparamagnetic Beads and Single Cells." Royal Society of Chemistry, July 10, 2015. https://doi.org/10.1039/C5LC00581G .
Publisher	Royal Society of Chemistry
Item record/more information	http://hdl.handle.net/10197/7883
Publisher's version (DOI)	10.1039/C5LC00581G

Downloaded 2025-09-01 21:36:19

The UCD community has made this article openly available. Please share how this access benefits you. Your story matters! (@ucd_oa)



© Some rights reserved. For more information

Micromagnet arrays for on-chip focusing, switching, and separation of superparamagnetic beads and single cells

S. Rampini,^a D. Kilinc,^a P. Li,^a C. Monteil,^a D. Gandhi,^a and G. U. Lee^{a,*}

Received 00th January 20xx,
Accepted 00th January 20xx

DOI: 10.1039/x0xx00000x

www.rsc.org/

Nonlinear magnetophoresis (NLM) is a powerful approach for on-chip transport and separation of superparamagnetic (SPM) beads, based on a travelling magnetic field wave generated by the combination of a micromagnet array (MMA) and an applied rotating magnetic field. Here, we present two novel MMA designs that allow SPM beads to be focused, sorted, and separated on-chip. Converging MMAs were used to rapidly collect the SPM beads from a large region of the chip and focus them into synchronized lines. We characterise the collection efficiency of the devices and demonstrate that they can facilitate on-chip analysis of populations of SPM beads using a single-point optical detector. The diverging MMAs were used to control the transport of the beads and to separate them based on their size. The separation efficiency of these devices was determined by the orientation of the magnetisation of the micromagnets relative to the external magnetic field and the size of the beads relative to that of micromagnets. By controlling these parameters and the rotation of the external magnetic field we demonstrated the controlled transport of SPM bead-labelled single MDA-MB-231 cells. The use of these novel MMAs promises to allow magnetically-labelled cells to be efficiently isolated and then manipulated on-chip for analysis with high-resolution chemical and physical techniques.

Introduction

Superparamagnetic (SPM) beads bearing affinity ligands have been applied in a number of lab-on-a-chip (LOC) biosensor and bioseparation systems.^{1–3} The advantage of using SPM beads in LOC devices is that highly efficient separation of an analyte from mL-scale volumes of a complex matrix, *e.g.*, serum or plasma, can be rapidly achieved without using a centrifuge or a chromatography system.⁴ In addition, the physical properties of the beads permit the direct detection of the analyte using an integrated optical or magnetic sensor.^{5–7} SPM beads have been successfully applied to capture, manipulate and detect cells,⁸ proteins,⁹ DNA and viruses.^{10–12} To maximise the capture efficiency and minimise reaction times, a concentration of *ca.* 10⁶ beads per ml is normally used to allow reactions to be completed on the order of minutes. It is often desirable to separate the beads carrying the target from unreacted beads to facilitate the detection of low concentrations of analytes or the isolation of rare cells. In the recent years, particular attention has been focused to the detection of very rare circulating tumour cells from blood, which has proven useful for the diagnosis of cancer, and a number of microfluidic devices have been described to achieve this aim.¹³ Among the different separation methodologies, SPM bead based sorting is attractive due to the possibility of simultaneous manipulation of cell populations, without the need of serial processing steps, such as multiple centrifugation or filtration passages, thus increasing the processing efficiency and decreasing the time required. Moreover, the

specificity of high-affinity SPM bead based separation promises to allow subtle differences in a particular cell type to be detected in a reliable manner. On-chip magnetic bead sorting methods based on patterned permanent magnets,^{14, 15} hydrodynamic flow,¹⁶ or complex channel geometries¹⁷ have been previously demonstrated.

Conventional magnetic separation involves the application of a magnetic field and field gradient to SPM beads suspended in a sample with a single magnet. The magnetic moment of the SPM beads, approximated as point dipoles, is proportional to the magnetic field strength \vec{H} ,

$$\vec{m} = \chi V \vec{H}, \quad (1)$$

where χ is the magnetic susceptibility of the beads, which is much higher than the susceptibility of the surrounding medium, and V is the bead volume. Such a bead possesses a magnetic potential energy expressed by the formula

$$U_m = -\mu_0 \vec{m} \cdot \vec{H} = -\frac{1}{2} \mu_0 \chi V \vec{H}^2, \quad (2)$$

where μ_0 is the magnetic permeability of free space and \vec{H} is the net field evaluated at the bead's centre. The beads are attracted towards regions of minimum potential energy, which obviously correspond to regions of magnetic field maxima. In conventional magnetic separation, the field generated by an external magnet leads to the motion of the SPM beads towards the maximum magnetic field. The induced motion of the beads is determined by their properties such as size and magnetic susceptibility, as evident from Eqs. 1 and 2, thus allowing for the separation of different bead populations.¹⁶ A limitation of this approach is the induced aggregation of the beads due to the dipole-dipole interactions that occur when a magnetic field is applied to reasonably high concentrations of beads. The formation of these bead aggregates leads to a very low separation efficiency.

^a Bionanoscience Group, School of Chemistry and Chemical Biology, UCD, Dublin, Ireland.

* Corresponding author. Tel +353 1716 2399; Fax +353 1 716 1178; e-mail gilullee@gmail.com
Electronic Supplementary Information (ESI) available: Additional videos. See DOI: 10.1039/x0xx00000x

Nonlinear magnetophoresis is a powerful new approach to transport and separate SPM beads based on their specific size and magnetisation that overcomes some of the limitations of linear magnetophoresis.^{18, 19} In this technique, a rotating magnetic field is superimposed on the local magnetic field produced by a rectilinear array of μm -size permanent magnets (micromagnet array, MMA) that are separated by μm -scale gaps. This produces multiple field maxima of the dimension of the beads, which minimises the bead-bead aggregation for $\chi < 1$.²⁰ The rotation of the external magnetic field creates a travelling wave of field that transports the beads across the chip at the speed of rotation. Size and magnetisation-based separation can be achieved by increasing the frequency of the travelling magnetic field to a speed where the hydrodynamic force exceeds the magnetic force.^{18–21} A critical frequency, ω_c , exists for a SPM bead

$$\omega_c = \frac{\chi\mu_0\sigma_0(H_{ext})}{18\eta} (2\pi\beta)^2 e^{-2\pi\beta}, \quad (3)$$

where σ_0 is the effective magnetic moment of the micromagnets, η is the viscosity of the surrounding medium, and β is the ratio between the bead's radius, r , and the centre-to-centre distance between adjacent magnets, d . The critical frequency is the frequency at which the average velocity of the beads starts to differ from the average velocity of the translating magnetic field, $\omega d/2\pi$. The advantages of the NLM separation technique are four-fold: high-resolution separation, parallel separation on the $\text{ca. } 10^5$ micromagnets per cm^2 , no fluid consumption, and the capacity to work with high bead densities. The combination of MMA and rotating fields has been used for on-chip cell manipulation.^{22–24} Using engineered microstructures, the controlled transport, assembly, and isolation of both labelled and non-labelled cells have been recently demonstrated.^{23, 24} The isolation of magnetically-labelled exosomes, recently identified extracellular organelles that contain RNA, has also been demonstrated using NLM.²⁰ Bead trajectories can be tuned by properly adjusting the design of the MMA or the orientation of the applied rotating field.^{25, 26} The capabilities of this separation technique, in terms of resolution, efficiency, and potential for multiplexing, make it an attractive option for bead-based LOC devices.

In this article, we present novel MMA designs for focusing and separating SPM beads based on non-rectilinear array geometries. The MMAs were designed to collect the beads dispensed on the array and organise them in single files, thus facilitating the integration of the NLM technology with optical or magnetic detection systems. In addition, we demonstrate that diverging arrays enabled programmable control over the trajectory of the beads. A tri-magnet junction was used to induce a preferential direction for the bead motion by tuning the orientation of the MMA magnetisation, thus enabling "magnetic switch" functionality. The size dependent switching behaviour of the SPM beads at these tri-magnet junctions was utilised for rapid and continuous separation of different bead populations without the need for changing the external magnetic field rotation frequency or hydrodynamic flow. The bead focusing and guiding capabilities of the device were used to control the transport of a magnetically-labelled MDA-MB-231 cell, as a proof of concept for on-chip single cell manipulation and analysis. The MMA designs presented here constitute essential building blocks for programmable micromagnet networks, aiming towards a multi-functional miniaturised bio-analytical device.

Results and Discussion

SPM Bead Focusing

Two MMA designs are presented in this work (Fig. 1) for the collection and focusing of magnetic beads. Each of these designs is comprised of three regions: region **1** is used to capture a large number of SPM beads from a sample and consists of a rectilinear MMA of 5 μm -diameter circular magnets with 8 μm centre-to-centre distance; region **2** is used to focus the beads and consists of lines of magnets tilted by $\pm 7^\circ$ with respect to the x -axis; and region **3** is composed of a single row of micromagnets where optical detection of the beads would take place. In design **A**, region **2** consists of densely packed lines of magnets (Fig. 1a); whereas in design **B**, region **2** consists of a tree-like structure in which the focusing process takes place in consecutive steps (Fig. 1h).

Bead transport was monitored on arrays magnetised in the x -direction in the presence of an external magnetic field rotating clockwise in the xz -plane (θ_{xz}) (Fig. 1b–d and 1i–k; Movies **S1** and **S2**). The applied field was kept lower than 100 Oe to avoid demagnetising the micromagnets. The two architectures were characterised by dispensing uniform SPM beads on region **1** and following their motion across the MMA using a microscope equipped with a motorised stage. In design **A**, the beads travelled across region **1** in the x -direction until they met the converging lines of micromagnets in region **2** (Fig. 1b–c). Due to the geometry of the MMA, beads entered region **2** with different y -coordinates (depending on their initial capture position) and were rapidly "focused". The percentage of focused beads increased with increasing distance from the beginning of region **2**, as shown in Fig. 1b–d. Once the beads reached the central line of micromagnets they remained confined in that row (Fig. 1d), until they entered region **3**. A similar behaviour was observed for design **B** where the beads rapidly moved through region **1** and were focused in region **2** (Fig. 1i–k).

The bead focusing efficiency was defined as the ratio of "focused" beads to the initial number of beads counted on region **1**. In design **A**, this was measured by counting the beads travelling within one magnet distance from the central line. In design **B**, the beads dispensed on the left hand-side of a particular focusing junction were counted, and the beads passing through that junction were defined as "focused" (light grey area in Fig. 1h). The focusing efficiencies of designs **A** and **B** were $94.3 \pm 2.9\%$ and $89.4 \pm 2.9\%$, respectively. The focusing efficiency of design **B** was limited by the small fraction of beads immobilised on what appeared to be defective micromagnets in this rather sparse array. The redundancy offered by the continuous array of magnets in design **A** reduced the impact of these imperfections, resulting in a lower probability for the immobilised beads to block the focusing process. The efficiency of these designs was also limited by the rate of transfer of the beads from the last micromagnet on the tilted rows to the central row (design **A**) or to the straight lines (design **B**) of micromagnets. This final focusing step was achieved with either a diamond or trimeric set of micromagnets that are presented in Fig. 1e and 1l, respectively. The diamond shaped configuration of micromagnets was observed to produce a lower transfer rate and they had a tendency to transfer the beads away from the central row of micromagnets into the adjacent row of converging micromagnets.

Insight into the focusing process in the diamond and tri-magnet configurations was gained from finite element simulations of the potential energy distributions on these geometries as a function of θ_{xz} , as presented in Fig. 1e and l. The deep blue and red regions

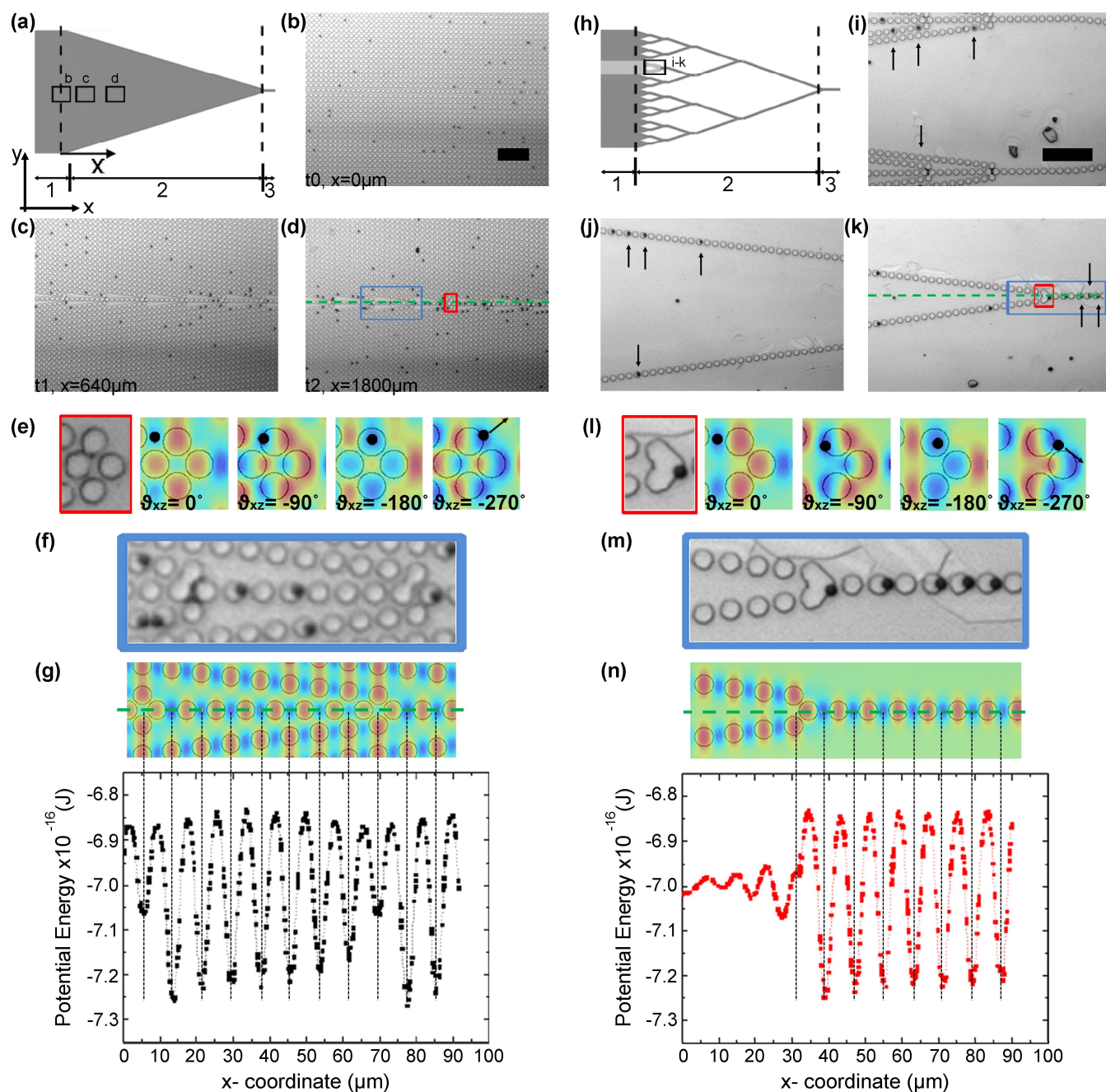


Fig. 1 Focusing MMA designs. (a) Design **A** consists of a continuous array of $5\ \mu\text{m}$ circular micromagnets (region 1), followed by parallel lines of magnets tilted by $\pm 7^\circ$ with respect to the horizontal axis of the chip (region 2). (b-d) Microscope images of the focusing process in design **A** (images correspond to the boxed areas in (a)). Also see Movie S1. The boxed areas in (d) correspond to the diamond junction between the tilted lines and the central row of magnets (red) and to the magnet array in which the potential energy landscape was simulated (blue). (e) 7.5 \times magnified image of the diamond junction (red), the simulation of the potential energy at a diamond junction for different phase angles of the applied field, and the corresponding expected positions of a travelling magnetic bead (black circles). The arrow indicates the predicted direction of bead motion. (f) 6 \times magnified image of the magnet array in which the potential energy landscape was simulated. (g) Simulation of the potential energy along the central row of magnets (boxed area in (d) along the green dashed line). The simulations were performed by imposing a micromagnet magnetisation of $80\ \text{kA/m}$ and an external field with a flux density of $30\ \text{G}$. (h) Design **B** consists of a continuous array of $5\ \mu\text{m}$ circular micromagnets, followed by a tree-like structure. (i-k) Focusing process on design **B** with the beads (arrows) leaving region 1 (i), travelling along the tilted lines of magnets (j), and crossing a focusing junction (k). Also see Movie S2. The boxed areas in (k) correspond to the tri-magnet focusing junction (red) and to the magnet array in which the potential energy landscape was simulated (blue). (l) 4.5 \times magnified image of the tri-magnet junction (red), the simulation of the potential energy at a tri-magnet junction for different angles of the applied field, and the corresponding expected positions of a travelling magnetic bead (black circles). The arrow indicates the anticipated direction of bead motion. (m) 4 \times magnified image of the array in which the potential energy landscape was simulated. (n) Simulation of the potential energy across a focusing junction (boxed area in (k) along the green dashed line). The magnitude of the potential energy minimum increased towards the tri-magnet junction and remained constant as it followed the periodicity of the array. Scale bars = $50\ \mu\text{m}$.

correspond to the locations of low and high potential energy, respectively. Black circles of the size of a SPM bead are placed on potential energy minima that represent the most likely position of the beads being focused from the positive y -direction. The spatial arrangement of the diamond shaped micromagnets, presented in Fig. 1e, created an energy distribution that forced the beads towards the next line of tilted micromagnets at $\vartheta_{xz} < 270^\circ$ (arrow points at the direction that the potential energy minimum moves as the external magnetic field is rotated). In contrast, at the tri-magnet junction the beads move across the micromagnets without encountering an energy barrier (Fig. 1l).

The converging MMA designs were further characterised by measuring the critical frequencies and velocities of uniform SPM beads. The critical frequency, ω_c , was measured for all regions of the MMA designs and was found to be 20–22 Hz except for the diamond-shaped junction in design **A** and the tri-magnet junction in design **B**. This indicated that the local potential energy landscape produced by a single line of micromagnets was similar to that produced by a rectilinear continuous array of micromagnets. This observation was confirmed by the 3-D finite element simulations of the potential energy along the central line of magnets in design **A** and at the focusing junction in design **B** (green dotted lines in Fig. 1d and 1k, respectively), shown in Fig. 1f and 1m, respectively. The potential energy minima for design **A** (Fig. 1g) and design **B** (Fig. 1n) were similar in magnitude. Along the central line of design **A**, the potential energy minima with the lowest magnitude occurred where the tilted lines met the central line. The potential energy

minima adjacent to this (in the $+x$ -direction) had the highest magnitude, where the magnitudes of the subsequent minima decreased with increasing x with a periodicity of eight micromagnets (Fig. 1f). In design **B**, this effect was also present at the end of region **1** (Fig. 1h), but not when the micromagnets converged at the tri-magnet junction (Fig. 1j). In both design **A** and **B**, the measured ω_c corresponded to a maximum bead velocity of ca. 180 $\mu\text{m/s}$ in region **1** and along the tilted lines of magnets. However, the speed of the overall focusing process was limited by the maximum velocity at which the beads were able to reach the central line (design **A**) or to cross a focusing junction (design **B**). The bead velocity at a diamond-shaped junction in design **A** was 88–96 $\mu\text{m/s}$ and slightly lower at a tri-magnet junction in design **B**.

Magnetic Switching Junction

Figure 2 illustrates the motion of the SPM beads through a switching junction, where a single line of micromagnets diverges into two lines of micromagnets at the tri-magnet structure. The schematics on the left-hand side of Fig. 2 show the orientation of the micromagnet magnetisation in the xy -plane (α), as well as the orientation of the rotation of the external magnetic field (ϑ_{xz}). When the magnetisation of the micromagnets was aligned with the x -axis, it was observed that the beads randomly selected one of the two diverging lines of micromagnets (data not shown), which we designate as $+$ or $-$ according to the angle they make with the x -axis. However, when the micromagnets were magnetised at an angle α with the x -axis, a preferential switching direction was imposed to the beads (movie **S3**). Fig. 2a, b, c, and d present four

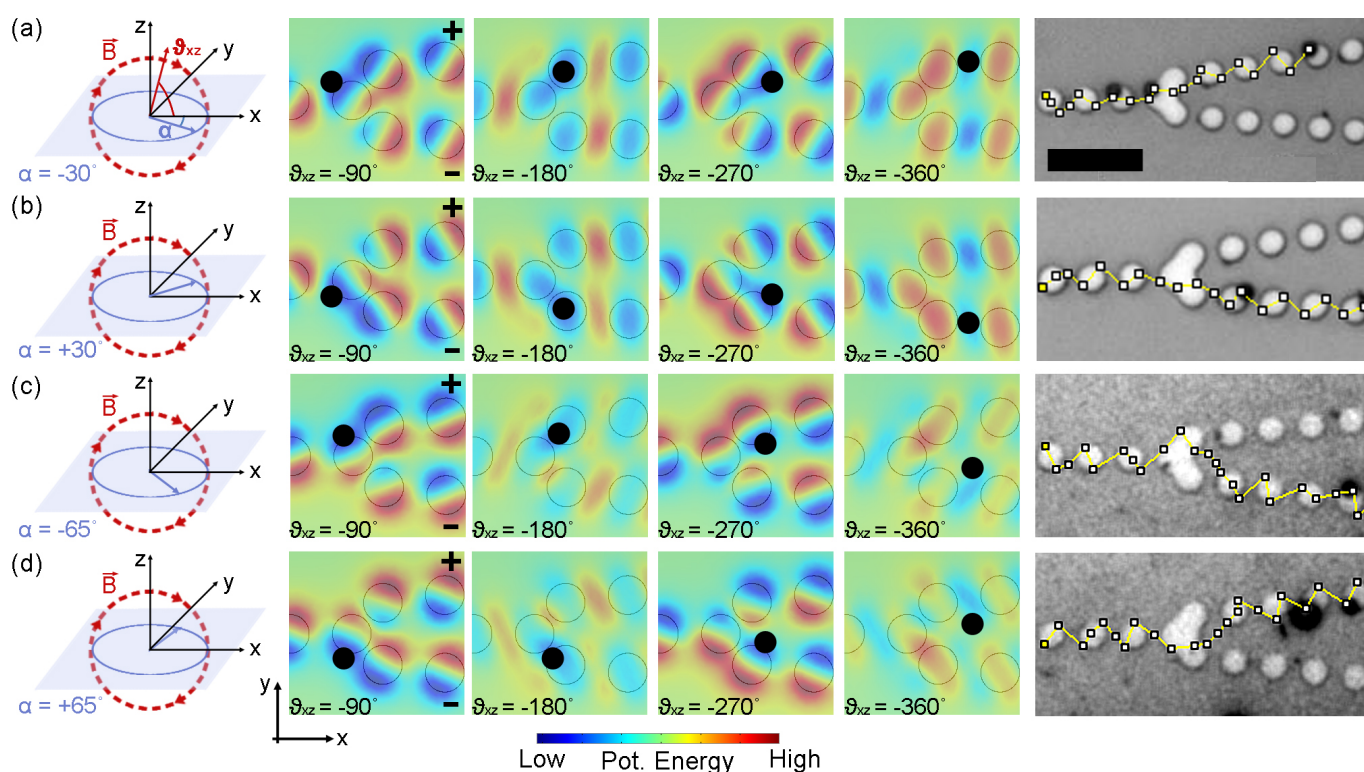


Fig. 2 Magnetic switching junction. Schematics (left column) identify the orientation of magnetisation of the micromagnets, α , and the sense of rotation of the applied field, ϑ_{xz} . The finite element calculations (false colour images) were performed by imposing a micromagnet magnetisation of 80 kA/m and an external field with flux density of 30 G. The black circles represent the predicted positions of the beads for given ϑ_{xz} . Microscopic images (right column) were used to identify the motion of the beads over the array and their trajectories were illustrated using white dots (representing specific ϑ_{xz}) connected with yellow lines. (a) For negative α , the beads travel from the bottom of a micromagnet to the top of the adjacent one and, therefore, approach the junction from the top. For low α values (-30°), the beads continue to travel along the $+$ direction. (b) For positive α , the beads travel from the top of a micromagnet to the bottom of the adjacent one and, therefore, approach the junction from the bottom. For low α values ($+30^\circ$), the beads continue to travel along the $-$ direction. (c) For $\alpha = -65^\circ$, the beads move onto the $-$ direction, after crossing the junction. (d) For $\alpha = +65^\circ$, the beads move onto the $+$ direction, after crossing the junction. Scale bar = 20 μm .

specific cases where $\alpha = -30^\circ$, 30° , -65° , and 65° , respectively. Tuning the orientation of the magnetisation of the micromagnets induced a preferential switching behaviour of the beads at the tri-magnet junctions.

To gain insight into this behaviour, finite element calculations were performed on the switching junction for the different values of α . Figure 2 presents the bead trajectories and potential energy landscapes for different α angles and ϑ_{xz} , with the deep blue regions in simulations corresponding to the potential energy minima. Black circles of the size of the SPM beads have been placed in the area of minimum potential energy for each α and ϑ_{xz} . There was agreement between the predicted motion based on the potential energy calculations and the observed motion of the beads (microscopic images on the right-hand side). For $\alpha < 0$, the beads jumped from the bottom of one micromagnet to the top of the adjacent one as the external field was rotated (*i.e.*, as ϑ_{xz} decreased). Accordingly, the beads moved across the top of the tri-magnet junction, and for small magnitudes of α , *e.g.*, $\alpha = -30^\circ$, they had a tendency to select the + line of micromagnets, as presented in Fig. 2a. Note that bead trajectories are superimposed on the microscopic images (yellow lines) to demonstrate this transport process. An opposite switching behaviour was observed when the magnetisation of the micromagnets was positively tilted, *e.g.*, $\alpha = +30^\circ$, where the beads selected the – direction after crossing the junction (Fig. 2b). This switching behaviour was modified for higher magnitudes of α , *i.e.*, the beads moved onto the – line of micromagnets for $\alpha = -65^\circ$ (Fig. 2c) and onto the + line of micromagnets for $\alpha = +65^\circ$ (Fig. 2d). This behaviour was interpreted as the result of the formation of an asymmetric potential energy distribution on the MMA at $\vartheta_{xz} = -360^\circ$.

Figures 3a and b present finite element calculations of the magnetic potential energy for a $2.8 \mu\text{m}$ diameter bead with $\chi = 0.17$, evaluated at the tri-magnet junction along the two possible trajectories, *i.e.*, $\vec{r}_1(+)$ and $\vec{r}_2(-)$, for $\alpha = -30^\circ$ and -65° , respectively. The potential energy was evaluated at $\vartheta_{xz} = -357.5^\circ$, which was the approximate angle at which the beads were observed to choose one of the two possible trajectories. For $\alpha = -30^\circ$ (Fig. 3a) the beads saw a lower potential energy profile along the \vec{r}_1 direction compared to the \vec{r}_2 direction. Thus, the force attracting the beads in the \vec{r}_1 direction ($-\partial U_m/\partial \vec{r}_1$) was higher than the force attracting the beads in the \vec{r}_2 direction ($-\partial U_m/\partial \vec{r}_2$). Thus, in this case the beads travelled along the \vec{r}_1 direction and continued along the + path. For $\alpha = -65^\circ$ (Fig. 3b), the beads saw a deeper and closer potential energy minimum in the \vec{r}_2 direction relative to the \vec{r}_1 direction. Accordingly, the beads travelled along the \vec{r}_2 direction, provided that they could overcome the short-range energy barrier that is formed along this trajectory. It was observed that this energy barrier imparted a frequency dependent switching behaviour to the switching process, *i.e.*, beads moving at low speed (external driving frequency $\omega < 1$ Hz) travelled along \vec{r}_1 , whereas beads moving at high speed ($\omega \geq 1$ Hz) travelled along \vec{r}_2 . Similar behaviour was observed for positive values of α .

Fig. 3c presents the percentage of beads travelling along the two micromagnet paths as a function of α , based on data collected over 10 different junctions on two separate chips, with at least 20 beads analysed per junction. The external driving frequency was 1 Hz, corresponding to a bead's velocity of $8 \mu\text{m/s}$. The switching efficiency (defined as the percentage of beads selecting the expected path) for the + path increased for decreasing negative values of α , and was effectively 100% for $-45^\circ < \alpha < -15^\circ$. Conversely, the percentage of beads taking + path decreased for

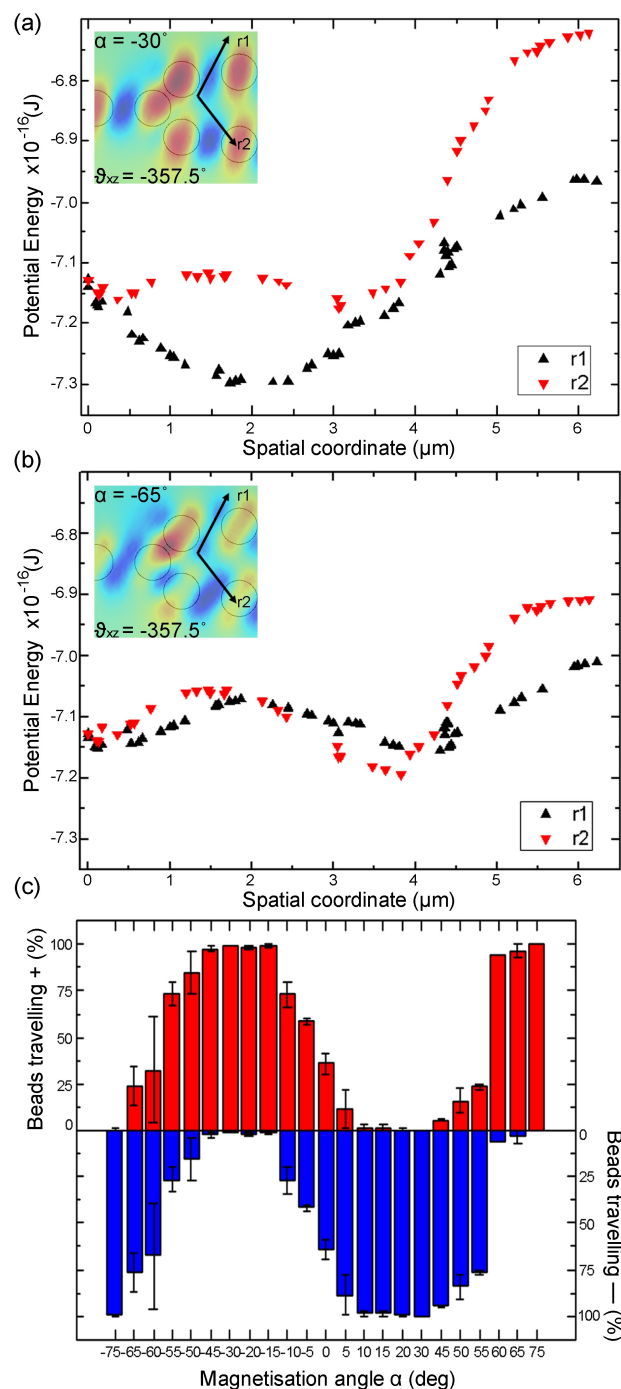


Fig. 3 Analysis of the switching behaviour of the tri-magnetic junction as a function of the orientation of magnetisation. (a,b) Simulated potential energy landscape of $2.8 \mu\text{m}$ beads evaluated along the two possible trajectories, \vec{r}_1 and \vec{r}_2 , for $\alpha = -30^\circ$ and for $\alpha = -65^\circ$. These simulations were performed at the centre of the bead, *i.e.*, in a plane $\Delta z = 2 \mu\text{m}$ above the micromagnets, for a micromagnet magnetisation of 80 kA/m and an external field with a flux density of 30 G . For $\alpha = -30^\circ$, the beads encountered a lower potential energy minimum along \vec{r}_1 , and travelled along that direction (+). For $\alpha = -65^\circ$, the beads encountered a deeper and closer potential energy minimum along \vec{r}_2 , and therefore chose the – direction, provided that they had sufficient kinetic energy to overcome the potential energy barrier at $1.5 \mu\text{m}$. (c) Percentage of $2.8 \mu\text{m}$ beads travelling along the + (red) and – (blue) directions for different magnetisation angles. The external driving frequency was 1 Hz . For negative α , the percentage of beads turning to the + direction increased until -45° . From $\alpha = -45^\circ$ to -65° the beads started to select the micromagnets in the – direction. For $\alpha < -65^\circ$ all beads moved onto the – direction after crossing the junction. The symmetric behaviour was observed for positively increasing α .

increasing positive values of α , with minimum values obtained for $15^\circ < \alpha < 45^\circ$. Further increasing $|\alpha|$ resulted in the inversion of the turning behaviour, such that the beads started to move to the opposite path after crossing the junction. Thus, for $-65^\circ < \alpha < -45^\circ$ the switching efficiency decreased with an increasing fraction of beads moving onto the $-$ direction. The opposite behaviour was observed for $45^\circ < \alpha < 60^\circ$, with an increasing fraction of beads moving onto the $+$ direction. The switching efficiency increased for even higher $|\alpha|$, i.e., for $\alpha < -65^\circ$, the percentage of beads taking the $-$ path was $> 95\%$, and for $60^\circ < \alpha$, the percentage of beads taking the $+$ path was $> 90\%$. However, at such high angles, the motion of the beads across the MMA was not smooth and the transport efficiency was reduced.

Bead Separation

The switching field produced by the tri-magnet junction was also used to separate SPM beads based on their size for certain α values. Figure 4 presents micrographs of a separation process in which 2.8 and 5.5 μm diameter beads were channelled to the $+$ and $-$ micromagnet paths, respectively, for $\alpha = -50^\circ$ (also see movie S4).

Here, small beads took the $+$ path, as expected from the previous characterisation, while the larger beads moved onto the $-$ path. The size-selective separation was characterized in the $10^\circ < |\alpha| < 70^\circ$ range, and the highest separation efficiency was achieved at $45^\circ < |\alpha| < 55^\circ$.

Figures 4a and 4b present the calculated potential energy landscape evaluated at $\Delta z = 2 \mu\text{m}$ and $3.35 \mu\text{m}$, respectively, as a function of ϑ_{xz} . The separation appears to occur due to the difference in the potential energy landscapes encountered by the small and large bead as the orientation of the external magnetic field rotates from -345° to -30° . The $2.8 \mu\text{m}$ beads encounter a potential energy barrier along the $-$ direction (\vec{r}_2) and a lower energy minimum along the $+$ direction (\vec{r}_1) (Fig. 4c). They therefore remain confined in the \vec{r}_1 trajectory. These calculations revealed that the $5.5 \mu\text{m}$ beads encounter a lower energy minimum along \vec{r}_2 , and thus take the $-$ direction (Fig. 4d). Figure 4e presents the results of the size-selective bead separation for the 2.8 and 5.5 μm beads moving across a tri-magnet junction for $\alpha = -50^\circ, 0^\circ$, and 50° . These results were used to calculate a separation efficiency $\epsilon = 1 - f_{5.5\mu\text{m}} - f_{2.8\mu\text{m}}$.

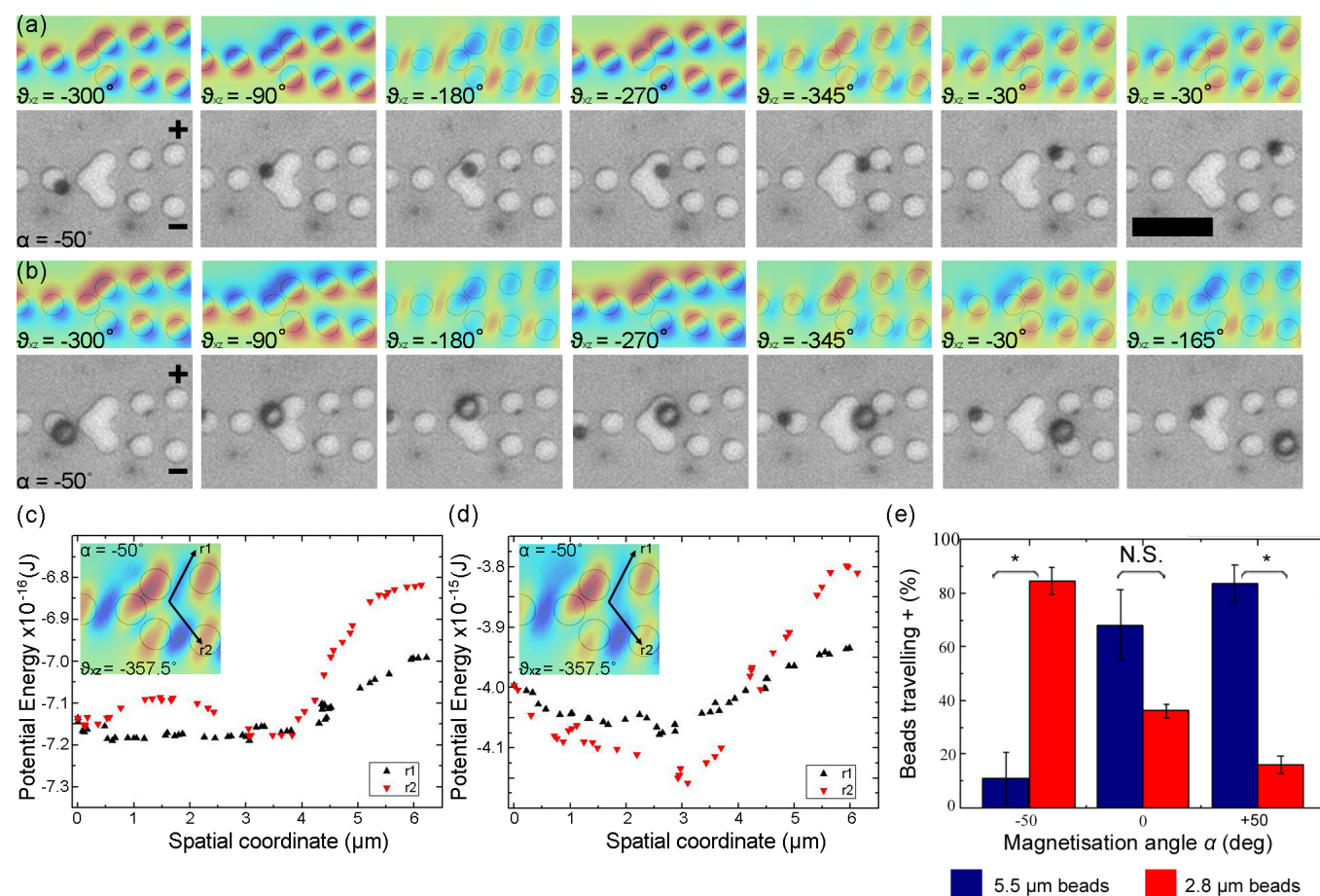


Fig. 4 SPM bead separation on a tri-magnet junction for a magnetisation angle $\alpha = -50^\circ$. (a) Finite element calculations as a function of ϑ_{xz} showing the evolution of the potential energy at a tri-magnet junction (z -plane = $2 \mu\text{m}$ above the MMA) for $\chi = 0.17$. The micrographs show the motion of a $2.8 \mu\text{m}$ SPM bead across the array as a function of ϑ_{xz} . The bead was observed to travel along the $+$ direction after crossing the tri-magnet junction, due to the lower potential energy minimum along this direction. (b) Finite element calculations showing the evolution of the potential energy at a tri-magnet junction (z -plane = $3.35 \mu\text{m}$ above the MMA), and micrographs showing the motion of 5.5 and $2.8 \mu\text{m}$ SPM beads. The $5.5 \mu\text{m}$ bead travelled along the $-$ direction after crossing the tri-magnet junction while the $2.8 \mu\text{m}$ bead continued to travel along the $+$ direction. (c) Potential energy landscape calculated for the $2.8 \mu\text{m}$ beads along the \vec{r}_1 and \vec{r}_2 directions at the critical $\vartheta_{xz} = -357.5^\circ$. The beads encounter an energy barrier along \vec{r}_2 at $1.5 \mu\text{m}$ that does not exist along the \vec{r}_1 trajectory. Thus, the $2.8 \mu\text{m}$ beads travel along the \vec{r}_1 trajectory although the potential energy landscape is relatively flat between 0.5 and $3 \mu\text{m}$. (d) Potential energy landscape for the $5.5 \mu\text{m}$ beads evaluated along the two possible directions \vec{r}_1 and \vec{r}_2 . The beads encounter a lower potential energy minimum along \vec{r}_2 and thus travel along that trajectory. (e) Fractions of $2.8 \mu\text{m}$ and $5.5 \mu\text{m}$ beads turning to the $+$ direction for different magnetisation angles. * $p < 0.05$; N.S. not significant (t-test). Error bars represent the standard error of the mean. Scale bars = $20 \mu\text{m}$.

where $f_{5.5\mu\text{m}}$ and $f_{2.8\mu\text{m}}$ are the fractions of beads, not turning to the predicted direction. In the case of $f_{5.5\mu\text{m}}$ this fraction was 0.11 and 0.16 for $\alpha = -50^\circ$ and $+50^\circ$, whereas in the case of $f_{2.8\mu\text{m}}$ it was 0.04 and 0.23 for $\alpha = -50^\circ$ and $+50^\circ$, respectively. The separation efficiency was determined to be $85.0 \pm 12.3\%$, $26.6 \pm 18.8\%$, and $60.6 \pm 7.8\%$ for $\alpha = -50^\circ$, 0° , and 50° , respectively. The difference in ϵ obtained at $\alpha = -50^\circ$ and 50° was attributed to local imperfections in the MMAs. These results suggest that the tri-magnet dimensions can be modified to achieve optimal separation efficiencies for a range of bead sizes and magnetisations.

Our bead separation results suggest that a sequential arrangement of multiple switching junctions would enable the continuous separation of multiple bead populations from each other. This approach has a number of advantages over existing techniques developed for on-chip separation of magnetic beads. First, using tri-magnet junctions, the beads can be separated simultaneously and continuously – a major advantage over bead separation based on differences in the critical frequency,^{18–21} which would require consecutive adjustments of the field driving frequency to achieve multiplex separation. Second, tri-magnet junctions do not require a fine tuning of the driving frequencies of the applied field, as in the case for recently-demonstrated multi-frequency driven systems.^{27, 28} These systems transport differently-sized beads in opposite directions (or selectively immobilize beads of particular size) by applying in-plane and out-of-plane magnetic fields rotating at different frequencies. In such systems the separation of the beads would take place over several cycles of field rotation and requires the fine-tuning of the ratio of driving frequencies, which are not the case for the tri-magnet junctions. The directionality imparted to the beads by the tri-magnet junctions introduces an additional degree of control on the transport of the beads towards specific regions of the chip, integrated to the separation process. Finally, the local field distribution generated by the tri-magnet junction eliminates the need for a precise synchronization of the external field orientation to achieve separation, as it was the case for previously reported loop pathways²⁹ and zig-zag sorting structures.³⁰

Programmed Manipulation of Single Cells

The capacity to control the direction of SPM bead motion may be used to transport beads and biological samples labelled with SPM beads to specific regions on a LOC device. As a proof-of-concept, we demonstrated the controlled transport of MDA-MB-231 breast carcinoma cells labelled with $1\mu\text{m}$ magnetic beads (Fig. 5 and movie S5). The NLM device was first used in the forward operation to transport the cell from region 1 of the MMA through a focusing junction. Then the orientation of rotation of the external magnetic field was inverted and the reverse operation of the device was used to guide the labelled cell along a pre-programmed direction across the same junction. The path taken by the travelling cell was controlled by orienting the magnetisation of the micromagnets at $\alpha = 30^\circ$. Figure 5a presents a schematic of the design of the experiment in which the cell was transported along a line of micromagnets from point i to iii using the rotating external magnetic field. At point iii, the sense of the rotating external magnetic field was reversed. Moving backward, the cell took to the - path and traversed the line of micromagnets through points iv and v. The cell transport process was monitored *via* time-lapse microscopy. Micrographs shown in Fig. 5b-f correspond to points i-v (in Fig. 5a). As predicted from the bead separation results, the cell labelled with the beads crossed the switch junction by taking the preferred - direction for $15^\circ < \alpha < 45^\circ$. This experiment demonstrated the transport of individual cells from one area of the

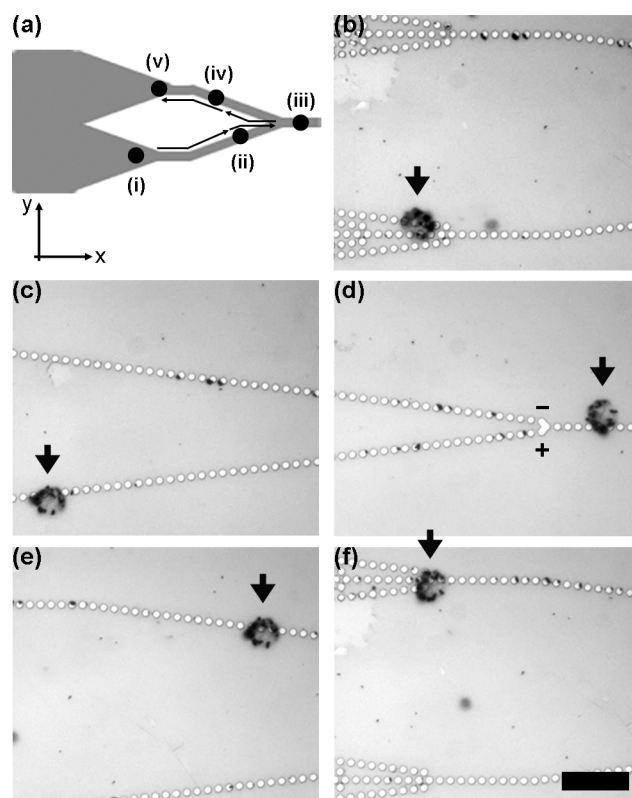


Fig. 5 Demonstration of the programmed transport of a single MDA-MB-231 cell labelled with $1\mu\text{m}$ SPM beads. (a) Schematic of the experiment in which the MDA-MB-231 cell was first focused and then guided back through a series of switches. (b-d) The cell (thick arrow) labelled with magnetic beads moves in the positive x-direction and crosses a focusing junction. (d-f) The orientation of the rotating external magnetic field is reversed to drive the cell backward. The cell chooses the - direction when crossing the junction for the second time, since the magnets were magnetised at $\alpha = 30^\circ$. Scale bar = $50\mu\text{m}$.

chip to another by simply adjusting the orientation of rotation of the external magnetic field for a pre-programmed magnetisation angle on the MMA. This feature may be incorporated in more complex networks of micromagnets to direct magnetically-labelled cells to specific regions of the chip, for subsequent biochemical analysis, and may be integrated with recently reported trapping stations²³ to create functional biosensors.

Conclusions

In this article we present novel micromagnet arrays designed to focus SPM beads (*via* two types of converging configurations), as well as size selective control of their motion (*via* a diverging configuration). The focusing experiments revealed that lines of micromagnets are almost as efficient as continuous arrays of micromagnets in terms of the speed and the total percentage of beads recovered. These focusing MMAs enabled the concentration of a specific fraction of beads into a single, synchronised line making it possible to analyse the beads based on a high-resolution, single-point optical detector. We have also demonstrated that tri-magnet junctions can be utilized to switch SPM beads onto specific paths and that under certain conditions these junctions are capable of separating SPM beads based on their size. By combining the focusing and switching elements, on-chip, manipulation of a single, magnetically-labelled cell was achieved with micron resolution. The reaction of cells labelled with SPM beads functionalised with one or

more antibodies will enable the highly efficient isolation of rare biological samples from complex fluids, such as blood, without exposing them to harsh separation conditions. In principle, MMAs can be designed using the elements described in this article to allow us to concentrate, separate, modify, and analyse the biological samples captured on the SPM beads. We anticipate that MMA chips designed using these elements as well as surface bound arrays will be capable of multiplexed analysis of biological targets, such as, exosomes, viruses, bacteria, or cells, isolated from complex media with near single molecule sensitivity.

Experimental

Chip fabrication. The micromagnet arrays were fabricated through a standard photolithographic process in a Class 100 cleanroom using S1813 positive photoresist (Shipley Microposit, Marlborough, MA) spin coated on a silicon wafer and irradiated with ultraviolet light (365 nm) at a dose of 60 mJ. The micromagnets were created via electron-beam metal deposition (Kurt J. Lesker Company, Hastings, UK). The structure of the micromagnets consisted of an initial 10 nm layer of chromium, followed by a 100 nm layer of cobalt, and another 10 nm layer of chromium. The bottom chromium layer enhances the adhesion of the magnets to the silicon substrate and the top layer protects the cobalt from oxidation. After the lift-off, the wafer was spin-coated with a 600 nm layer of spin-on-glass (Filmtronics, Butler, PA) and cured at 300°C for 3 h in a furnace under nitrogen environment. The micromagnets were then magnetised using a 11 kG impulse magnetiser (ASC Scientific, Carlsbad, CA). A goniometer with 1° resolution was used to set the magnetisation: the MMA chip was manually oriented along the desired directions to set the magnetisation angle of the micromagnets. For each magnetisation angle the bead transport at a tri-magnet junction was observed after multiple magnetisation/demagnetisation cycles of the MMA.

Experimental setup. The experimental setup was similar to those used in previous works from our group.^{20, 21} A magnetic field rotating in a plane parallel to the axis of motion of the beads was generated by three electromagnets arranged along mutually orthogonal axes. The solenoids were composed by 570 coils surrounding a cylindrical iron core (ASTM A536 ductile iron) 150 mm long and with diameter 60 mm. The sinusoidal signal necessary for a rotating field was created by a two channel function generator (Tektronix, Beaverton, OR) that produced two sinusoidal waves with a 90° phase difference. Two programmable amplifiers (Kepco, Flushing, NY) were used to amplify the signal and to supply it to the electromagnets for generating a magnetic field with flux density of 30 G in the x-direction and 35 G in the z-direction that was used consistently in all the experiments. Imaging was performed using an epi-illumination optical microscope (Zeiss Axioskop2, Welwyn Garden City, UK) equipped with a 20× objective and an high-speed camera (Axiocam, Hsm, Zeiss). The characterisation of the bead behaviour was performed with commercially available 2.8 µm beads (Invitrogen, Carlsbad, CA). Commercially available 5-5.9 µm beads (SpheroTech, Chicago, IL) were used to test how bead properties affected turning behaviour. In the simulations the diameter of the beads was considered 5.5 µm.

Finite element simulations. The simulations were performed imposing a magnetisation of the micromagnets of 80 kA/m along different orientations in the xy-plane, consistently with simulations in our previous works. The external field had a flux density of 30 G and it was applied rotating clockwise in the xz-plane.

Bead functionalization. The antibody functionalization was

performed on 1 µm carboxylated beads synthesised in our laboratory. The beads were re-suspended in MES buffer (2-(N-morpholino)ethanesulfonic acid) pH 6.1, at a concentration 10⁸ beads/ml. The beads were washed three times with MES buffer. A magnet rack was used to hold the beads during the washing steps. After being washed the beads were re-suspended in 500 µl MES buffer. 10 mg EDC (1-Ethyl-3-(3-dimethylaminopropyl-carbodiimide)) were dissolved in 1 ml MES buffer, and 10 mg sulfo-NHS (N-Hydroxysuccinimide) were as well dissolved in 1 ml MES buffer. 290 µl of the EDC solution and 290 µl of the NHS solution were added to the beads and they were briefly sonicated (three times 1 s sonication with 3 s intervals). Then, the solution was incubated for 15 min at room temperature on a rotating rack. After the incubation, the beads were washed once and re-suspended in 500 µl MES buffer. 50 µl of antiCD9 antibody (HansaBioMed, Tallinn, Estonia) having a concentration of 1 mg/ml was added to the beads. The solution was then incubated for 1 h at room temperature on a rotating rack and then moved at 4°C for an overnight incubation. The next day the beads were washed twice with PBST, re-suspended in 1 ml PBS buffer and stored at 4°C.

Cell targeting. MDA-MB-231 breast carcinoma cells were cultured in Dulbecco's Modified Eagle Medium (DMEM) supplemented with 1% Penicillin/Streptomycin and 10% foetal bovine serum. The cells were seeded in a T25 culturing flask and placed in a CO₂ supplied incubator at 37°C. Cells up to passage 5 were used in the experiments. For the labelling procedure the cells were detached from the culture flask using trypsin-EDTA (Gibco, Carlsbad, CA). The suspension was placed in a 15 ml tube and centrifuged at 900 rpm for 3 min to form a cell pellet. The culturing medium was replaced with PBS buffer and the cells were counted using a hemocytometer. The cell suspension was diluted and samples containing 10⁵ cells in 1 ml PBS buffer were prepared. 5×10⁶ magnetic beads were added to the each sample. The cells and the beads were incubated for 1h at room temperature on a rotating wheel. After the incubation, the microcentrifuge tubes containing the cells and the beads were brought to direct contact with a permanent magnet for 1 min, followed by a brief vortex shake. This step was performed in order to increase the binding probability. The binding was assessed by comparing antibody-coated beads with non-coated beads. When non-coated beads were used almost no binding between the beads and the cells was observed, whereas cells were covered with anti-CD9 coated beads.

Acknowledgements

The authors thank Alex von Kriegsheim for providing us with the MDA-MB-231 breast carcinoma cells and Victoria Matias for synthesising the SPM beads. This work was supported by the Science Foundation of Ireland (08/RP1/B1376; 08/IN1/B2072), Irish Research Council, and the Nanoremedies Programme funded under the Programme for Research in Third-Level Institutions and co-funded under the European Regional Development fund.

Notes and references

1. A. van Reenen, A. M. de Jong, J. M. J. den Toonder and M. W. J. Prins, *Lab on a chip*, 2014, 14, 1966-1986.
2. Q. Pankhurst, N. Thanh, S. Jones and J. Dobson, *Journal of Physics D: Applied Physics*, 2009, 42, 224001.

3. M. A. Gijs, F. Lacharme and U. Lehmann, *Chemical reviews*, 2010, 110, 1518-1563.
4. M. P. Marszałł, *Pharmaceutical Research*, 2011, 28, 480-483.
5. D. R. Baselt, G. U. Lee, M. Natesan, S. W. Metzger, P. E. Sheehan and R. J. Colton, *Biosensors & bioelectronics*, 1998, 13, 731-739.
6. M. M. Gijs, *Microfluid Nanofluid*, 2004, 1, 22-40.
7. A. Hecht, P. Kinnunen, B. McNaughton and R. Kopelman, *Journal of Magnetism and Magnetic Materials*, 2011, 323, 272-278.
8. N. Pamme and C. Wilhelm, *Lab Chip*, 2006, 6, 974-980.
9. L. Johansson, K. Gunnarsson, S. Bijelovic, K. Eriksson, A. Surpi, E. Gothelid, P. Svedlindh and S. Oscarsson, *Lab on a chip*, 2010, 10, 654-661.
10. Y.-F. Ran, C. Fields, J. Muzard, V. Liauchuk, M. Carr, W. Hall and G. U. Lee, *The Analyst*, 2014, 139, 6126-6134.
11. W. S. Chang, H. Shang, R. M. Perera, S. M. Lok, D. Sedlak, R. J. Kuhn and G. U. Lee, *The Analyst*, 2008, 133, 233-240.
12. J. Muzard, M. Platt and G. U. Lee, *Small*, 2012, 8, 2403-2411.
13. C. Wyatt Shields Iv, C. D. Reyes and G. P. Lopez, *Lab on a Chip*, 2015, 15, 1230-1249.
14. K. Hoshino, Y.-Y. Huang, N. Lane, M. Huebschman, J. W. Uhr, E. P. Frenkel and X. Zhang, *Lab on a Chip*, 2011, 11, 3449-3457.
15. C. W. Shields, C. E. Livingston, B. B. Yellen, G. P. López and D. M. Murdoch, *Biomicrofluidics*, 2014, 8, 041101.
16. N. Pamme and A. Manz, *Analytical chemistry*, 2004, 76, 7250-7256.
17. E. Ozkumur, A. M. Shah, J. C. Ciciliano, B. L. Emmink, D. T. Miyamoto, E. Brachtel, M. Yu, P. I. Chen, B. Morgan, J. Trautwein, A. Kimura, S. Sengupta, S. L. Stott, N. M. Karabacak, T. A. Barber, J. R. Walsh, K. Smith, P. S. Spuhler, J. P. Sullivan, R. J. Lee, D. T. Ting, X. Luo, A. T. Shaw, A. Bardia, L. V. Sequist, D. N. Louis, S. Maheswaran, R. Kapur, D. A. Haber and M. Toner, *Science translational medicine*, 2013, 5, 179ra147.
18. B. B. Yellen, R. M. Erb, H. S. Son, R. Hewlin Jr, H. Shang and G. U. Lee, *Lab on a Chip*, 2007, 7, 1681-1688.
19. B. B. Yellen and L. N. Virgin, *Physical Review E*, 2009, 80, 011402.
20. P. Li, D. Kilinc, Y.-F. Ran and G. U. Lee, *Lab on a Chip*, 2013, 13, 4400-4408.
21. P. Li, A. Mahmood and G. U. Lee, *Langmuir : the ACS journal of surfaces and colloids*, 2011, 27, 6496-6503.
22. A. Chen, T. Byvank, W. J. Chang, A. Bharde, G. Vieira, B. L. Miller, J. J. Chalmers, R. Bashir and R. Sooryakumar, *Lab on a chip*, 2013, 13, 1172-1181.
23. B. Lim, V. Reddy, X. Hu, K. Kim, M. Jadhav, R. Abedini-Nassab, Y.-W. Noh, Y. T. Lim, B. B. Yellen and C. Kim, *Nat Commun*, 2014, 5.
24. T. Henighan, A. Chen, G. Vieira, A. J. Hauser, F. Y. Yang, J. J. Chalmers and R. Sooryakumar, *Biophysical journal*, 2010, 98, 412-417.
25. M. A. Tahir, L. Gao, L. N. Virgin and B. B. Yellen, *Physical Review E*, 2011, 84.
26. S. Anandakumar, V. S. Rani, S. Oh, B. L. Sinha, M. Takahashi and C. Kim, *Biosensors & bioelectronics*, 2010, 26, 1755-1758.
27. P. Tierno, F. Sagues, T. H. Johansen and T. M. Fischer, *Physical Chemistry Chemical Physics*, 2009, 11, 9615-9625.
28. L. Gao, M. A. Tahir, L. N. Virgin and B. B. Yellen, *Lab on a chip*, 2011, 11, 4214-4220.
29. K. Gunnarsson, P. E. Roy, S. Felton, J. Pihl, P. Svedlindh, S. Berner, H. Lidbaum and S. Oscarsson, *Advanced materials*, 2005, 17, 1730-1734.
30. A. Torti, V. Mondiali, A. Cattoni, M. Donolato, E. Albisetti, A. M. Haghiri-Gosnet, P. Vavassori and R. Bertacco, *Applied Physics Letters*, 2012, 101, 142405.